On the different levels of dust attenuation to nebular and stellar light in star-forming galaxies

Yusei KOYAMA,[1,2,*] Rhythm SHIMAKAWA,[1] Issei YAMAMURA,[3] Tadayuki KODAMA,[4] and Masao HAYASHI[5]

[1]Subaru Telescope, National Astronomical Observatory of Japan, National Institutes of Natural Sciences, 650 North A'ohoku Place, Hilo, HI 96720, USA
[2]Graduate University for Advanced Studies (SOKENDAI), 2-21-1 Osawa, Mitaka, Tokyo 181-8588, Japan
[3]Institute of Space Astronautical Science, Japan Aerospace Exploration Agency, 3-1-1 Yoshinodai, Chuo-ku, Sagamihara-shi, Kanagawa 252-5210, Japan
[4]Astronomical Institute, Tohoku University, 63 Aramaki, Aoba-ku, Sendai, Miyagi 980-8578, Japan
[5]National Astronomical Observatory of Japan, 2-21-1 Osawa, Mitaka, Tokyo 181-8588, Japan

*E-mail: koyama@naoj.org

Abstract

As a science verification study of the newly released AKARI/FIS Faint Source Catalog ver. 1, this paper discusses the different levels of dust attenuation toward stellar light and nebular emission lines within local star-forming galaxies at $0.02 < z < 0.10$. By constructing an updated version of the AKARI–SDSS–GALEX matched galaxy catalog (with >2000 sources), we compare the dust attenuation levels toward stellar light (from the L_{IR}/L_{UV} ratio) and nebular emission lines (from the Hα/Hβ ratio). We find that there is a clear trend that more massive galaxies tend to have higher "extra" attenuation toward nebular regions, while galaxies with higher specific star formation rates tend to have lower extra attenuation. We also confirm these trends by using the WISE mid-infrared photometry with a significantly large sample size of the WISE–SDSS–GALEX galaxies (>50000 sources). Finally, we study how the levels of extra attenuation toward nebular regions change across the *SFR*–$M_\star$ plane. We find that, even at a fixed stellar mass, galaxies located *below* the main sequence tend to have higher levels of extra attenuation toward nebular regions, suggesting a change in dust geometry within the galaxies across the star-forming main sequence during the course of the star formation quenching process.

Key words: galaxies: evolution — galaxies: ISM — galaxies: star formation

1 Introduction

Measuring the star formation rate (*SFR*) of galaxies is always an important task in extra-galactic astronomy. A common approach to deriving *SFR* is to observe the rest-frame UV light from young massive stars, or to measure the nebular emission line fluxes such as the Hα ($\lambda = 6563\,\text{Å}$)

line associated with young star-forming regions, applying a proper dust attenuation correction (e.g., Kennicutt 1998; Kennicutt et al. 2009; Hao et al. 2011; Kennicutt & Evans 2012). Because star-forming regions are dust-rich environments in general, the light emitted from those young star-forming (H II) regions is known to be heavily obscured

by dust, and unfortunately dust attenuation correction has been one of the biggest sources of uncertainty when deriving the *SFR*s.

The Hα line is recognized as one of the best indicators of *SFR*. The dust attenuation at the Hα line can ideally be estimated by observing the Hβ ($\lambda = 4861\,\text{Å}$) line at the same time and translating the Hα/Hβ line flux ratio (Balmer decrement) to the dust attenuation levels with an assumption of reddening curves. Although it is true that even the Hα line could be heavily obscured in the case of extremely dusty sources (e.g., Poggianti & Wu 2000; Koyama et al. 2010), it is widely recognized that the dust-corrected Hα-based *SFR* is one of the most reliable estimators of *SFR*. The Hα line has been commonly used for *SFR* measurements of local galaxies, and with the recent improvements of near-infrared observational technologies, it has now become much easier to access the (redshifted) Hα line of distant galaxies across the environment (e.g., Geach et al. 2008; Garn et al. 2010; Sobral et al. 2013; Koyama et al. 2013; and many others).

However, because the Hβ line is much fainter than the Hα, it is still very challenging to directly measure the dust attenuation to the Hα line for a statistical sample of galaxies at high redshifts with the Balmer decrement; indeed, only a small fraction of high-redshift works successfully detect both the Hα and Hβ lines of individual sources for a statistical sample of galaxies (e.g., Shivaei et al. 2015; Reddy et al. 2015). An alternative approach exploited in many studies is to use the dust reddening derived from broadband spectral energy distribution (SED) fits to predict the dust attenuation to the Hα line. However, in addition to the well-known degeneracy between age, metallicity, and dust reddening in broad-band SEDs, this process suffers from a large uncertainty because the dust reddening estimated from broad-band SEDs indicates the reddening toward *stellar* light, while the reddening toward *nebular* emission lines could be different (e.g., Reddy et al. 2015; Koyama et al. 2015; Zahid et al. 2017).

It should be noted that nebular emission lines from H II regions tend to be more obscured by dust than the stellar continuum light averaged over the galaxies. Calzetti (1997) showed that stellar continuum light is a factor of ∼2× *less* reddened than the nebular emission lines on average, and established a relation between the color excess toward the stellar continuum and nebular emission lines with the equation $E(B - V)_{\text{star}} = 0.44 \times E(B - V)_{\text{gas}}$ (see also Calzetti et al. 1994, 2000). Although many studies have applied this relation to convert the reddening to stellar light to that of ionized gas until recently, it should be noted that the factor "0.44" in the above equation is derived as an average value of a wide variety of galaxy populations in the local universe (from starbursts to dwarfs; see Calzetti 1997),

and it would not be a number applicable to all types of galaxies.

Some recent studies suggest that the factor of this "selective" attenuation (or "extra" attenuation) toward nebular emission lines is different for distant galaxies (e.g., Erb et al. 2006; Reddy et al. 2010; Kashino et al. 2013; Pannella et al. 2015), and a growing number of high-*z* studies do not blindly assume the same relation as for local galaxies (e.g., Förster Schreiber et al. 2009; Wuyts et al. 2013; Tadaki et al. 2013; Theios et al. 2018). It is often argued that the different levels of attenuation toward ionized gas originates from the fact that stars and ionized gas do not occupy the same regions within the galaxies (e.g., Calzetti et al. 1994; Wild et al. 2011; Price et al. 2014; Reddy et al. 2015). The ionized gas requires the presence of young massive (short-lived) stars to ionize themselves (hence they are always located in the birth clouds), while stellar continuum light can also be contributed by long-lived, non-ionizing stars distributed throughout the galaxy— the so-called "two-component" dust model composed of birth-clouds and diffuse ISM as described by Charlot and Fall (2000). It is of great interest to understand what determines the levels of extra attenuation toward nebular regions—this is not only to reduce the uncertainties of *SFR* estimates, but also to understand the link between star and gas geometry inside the galaxies along the process of galaxy evolution.

A method to study the extra attenuation toward nebular regions would be to compare the $E(B - V)_{\text{gas}}$ and $E(B - V)_{\text{star}}$ measured independently. The $E(B - V)_{\text{gas}}$ can be measured with the Hα/Hβ ratio as described above, and the $E(B - V)_{\text{star}}$ can be estimated from the UV attenuation measured by the far-infrared (FIR) to UV luminosity ratio with an assumed attenuation curve. The key observational data is therefore deep mid-infrared (MIR)–FIR photometry covering a wide area on the sky to directly trace the dust thermal emission from galaxies. The Wide-field Infrared Survey Explorer (WISE: Wright et al. 2010) performed an all-sky survey at MIR (3.4, 4.6, 12, 22 μm; W1–W4), and provides an excellent tool for this purpose. Also, the AKARI (Murakami et al. 2007) Far-Infrared Surveyor (FIS: Kawada et al. 2007) performed an all-sky survey at 65, 90, 140, and 160 μm with high sensitivity and high angular resolution (Doi et al. 2015; Takita et al. 2015), and thus serves as another ideal tool for this purpose.

In Koyama et al. (2015) we constructed an AKARI–SDSS–GALEX star-forming galaxy sample by cross-matching the sources in the AKARI-FIS Bright Source Catalog ver. 1 (Yamamura et al. 2010) with SDSS (DR7) and GALEX (GR5) data. By comparing A_{UV} (derived from the $L_{\text{IR}}/L_{\text{UV}}$ ratio) and $A_{\text{Hα}}$ (derived from the Balmer decrement), we found a hint that more massive galaxies and/or

galaxies with low Hα equivalent widths ($EW_{H\alpha}$) tend to show higher levels of extra attenuation toward nebular regions. In this paper, as a science demonstration study of the newly released AKARI Faint Source Catalog ver. 1 (I. Yamamura et al. in preparation), we will revisit the issue of this extra attenuation toward nebular regions by constructing an updated version of the AKARI–SDSS–GALEX matched galaxy catalog.

This paper is organized as follows. In section 2 we present our new AKARI–SDSS–GALEX star-forming galaxy catalog with the newly released AKARI Faint Source Catalog (subsection 2.1), and derive their FUV-, Hα-, and FIR-based *SFR*s as well as the dust attenuation levels toward stellar and nebular emission (subsections 2.2– 2.4). In section 3 we investigate how the "extra" attenuation toward nebular regions changes with various galaxy properties using the AKARI–SDSS–GALEX sample. In section 4 we verify our results by using WISE data, as it also covers the whole sky and provides an independent measurement of IR-based *SFR*s. In section 5, by using our AKARI–SDSS–GALEX and WISE–SDSS–GALEX sample, we show how the levels of extra attenuation to nebular regions changes across the star-forming main sequence. In section 6 we describe caveats on the interpretation of our results by comparing the results when we use Hα-based *SFR*s instead of UV/IR-based *SFR*s. Finally, our conclusions are summarized in section 7. Throughout the paper, we adopt the cosmological parameters of $\Omega_M = 0.3$, $\Omega_\Lambda = 0.7$, and $H_0 = 70 \, \mathrm{km \, s^{-1} \, Mpc^{-1}}$, and we assume the Kroupa (2001) initial mass function (IMF). All magnitudes are given in the AB system.

2 New AKARI-SDSS-GALEX sample

2.1 Sample selection

In Koyama et al. (2015) we constructed a star-forming galaxy sample ($N = 1200$) in the local universe by matching the SDSS Data Release 7 (DR7: Abazajian et al. 2009) spectroscopic galaxy sample, UV sources from the All-sky Imaging Survey of GALEX fifth data release (GR5), and FIR sources from the AKARI FIS Bright Source Catalog ver. 1 (BSCv1: Yamamura et al. 2010). We refer readers to Koyama et al. (2015) for details of the source matching procedure, but we briefly describe here our sample selection process. We note that the dataset is the same as used in Koyama et al. (2015), except that we replace our FIR data from the AKARI FIS Bright Source Catalog ver. 1 with the newly released AKARI Faint Source Catalog ver. 1 (FSCv1: I. Yamamura et al. in preparation). The key observational quantities used in this paper are SDSS Hα and Hβ fluxes to derive Hα-based *SFR*s (subsection 2.2), and GALEX FUV

and AKARI FIR (90 μm and 140 μm) photometry to derive UV+FIR *SFR*s (subsection 2.3).

The first step is to match the SDSS (DR7) spectroscopic catalog with the FUV-detected sources selected from the GALEX (GR5) All-sky Imaging Survey (AIS) with the help of the SDSS (DR7)–GALEX (GR5) matched photometric catalog published by Bianchi et al. (2011).[1] We use the Max Planck Institute for Astrophysics and Johns Hopkins University (MPA/JHU) catalog[2] for spectroscopic measurements, including the Galactic extinction correction, stellar absorption correction for emission line fluxes, and stellar mass estimates for individual galaxies with SED fitting (Kauffmann et al. 2003; Salim et al. 2007). We restrict the sample to those within the redshift range of $0.02 < z < 0.10$, and we also apply a stellar mass cut of $\log(M_\star/M_\odot) > 8.5$. We further require detection of four major emission lines (Hα, [N II], Hβ, [O III]) to select star-forming galaxies using the "BPT" diagram (Baldwin et al. 1981), following the standard criteria to distinguish star-forming galaxies from AGNs (Kauffmann et al. 2003; Kewley et al. 2006). We thus select 78731 SDSS–GALEX sources satisfying all the above criteria.

We then match our SDSS–GALEX galaxy sample with the AKARI FIS Faint Source Catalog ver. 1 (hereafter FSCv1: I. Yamamura et al. in preparation). The AKARI FSCv1 contains 401157 point sources selected with a different detection policy from the AKARI FIS Bright Source Catalogs (ver. 1/ver. 2) to improve the sensitivity, particularly in the high ecliptic latitude regions where the number of scans is large (for details, see I. Yamamura et al. in preparation). We note that the majority of the AKARI sources are Galactic objects distributed along the Galactic plane, and we find that ∼15000 galaxies are located within the SDSS survey area. Considering the point spread function size of AKARI at 90 μm (∼40″), we use a 20″ radius aperture to search for counterparts, and find 2416 star-forming galaxies identified in the AKARI, SDSS, and GALEX catalogs, with a median redshift of $z = 0.043$, and with a median separation of 5″.1 (measured as the angular distance between the AKARI and SDSS coordinates).

In figure 1 (left) we compare the AKARI *WIDE-S* (90 μm) photometry from AKARI/FIS BSCv1 and FSCv1 for galaxies identified in both of the catalogs. A more detailed comparison between the catalogs will be presented in I. Yamamura et al. (in preparation), but we confirm here that the FIR flux measurements agree well between BSCv1 and FSCv1 over a wide flux range for local star-forming galaxies. We also show in figure 1 (right) the 90 μm flux distribution of the AKARI–SDSS–GALEX sample from

---

[1] ⟨https://archive.stsci.edu/prepds/bianchi_gr5xdr7/⟩.
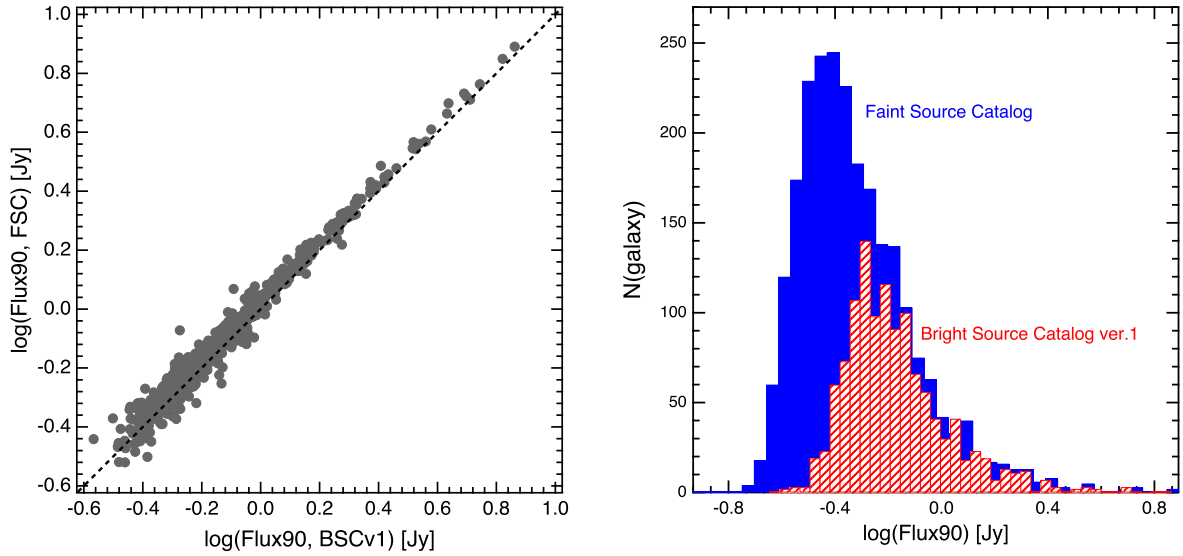
[2] ⟨https://wwwmpa.mpa-garching.mpg.de/SDSS/DR7/⟩.

Fig. 1. (Left) Comparison between AKARI/FIS *WIDE-S* (90 μm) flux densities from the Bright Source Catalog ver. 1 (BSCv1) and Faint Source Catalog ver. 1 (FSCv1) for star-forming galaxies at $0.02 < z < 0.1$ identified in both the catalogs, showing reasonable agreement between BSCv1 and FSCv1 over a wide flux range. (Right) Distribution of 90 μm flux densities (Flux90) for our old/new AKARI–SDSS–GALEX star-forming galaxy samples. The red (hatched) histogram shows the distribution of Flux90 for the AKARI(BSCv1) sample presented in our previous work (Koyama et al. 2015), while the blue (filled) histogram shows the result for our new AKARI(FSCv1) sample. This plot demonstrates that the number in our AKARI–SDSS–GALEX galaxy sample has been significantly increased, mainly at the faint end, with the improved sensitivity of the AKARI Faint Source Catalog. (Color online)

our previous version (with BSCv1; red hatched histogram) and the updated version of the catalog (with FSCv1; blue filled histogram). It is clear that the increase of the total sample size mainly comes from the improved sensitivity at $\log F_{90\,\mu\mathrm{m}} \lesssim -0.4$ [Jy].

2.2 Hα-based *SFR*s and dust attenuation toward nebular regions

The key physical parameters that we use in this study are Hα- and UV/FIR-based *SFR*s and dust attenuation toward stellar and nebular light for individual galaxies. We derive these quantities following basically the same method presented in Koyama et al. (2015), but here we provide a quick overview of the procedure.

To derive the Hα-based *SFR*s, we first calculate the dust attenuation at the Hα line by using the Hα/Hβ flux ratio (Balmer decrement) with the following equation, assuming Case B recombination at $T = 10^4$ K with an electron density of $n_e = 10^2$ cm^{-3}:

$$A_{\mathrm{H}\alpha} = \frac{-2.5\,k_{\mathrm{H}\alpha}}{k_{\mathrm{H}\alpha} - k_{\mathrm{H}\beta}} \log\left(\frac{2.86}{F_{\mathrm{H}\alpha}/F_{\mathrm{H}\beta}}\right), \qquad (1)$$

$$E(B-V)_{\mathrm{gas}} = A_{\mathrm{H}\alpha}/k_{\mathrm{H}\alpha}. \qquad (2)$$

We assume here the Cardelli, Clayton, and Mathis (1989) Galactic extinction curve to determine $k_{\mathrm{H}\alpha}$ and $k_{\mathrm{H}\beta}$ in the above equations, following the original derivation of the

Calzetti et al. (2000) relation (see, e.g., Steidel et al. 2014; Reddy et al. 2015; Shivaei et al. 2015). We emphasize that our conclusions are unaffected even if we apply the Calzetti et al. (2000) curve to both nebular and stellar light as assumed by many studies including our previous work (e.g., Garn & Best 2010; Sobral et al. 2012; Koyama et al. 2015), while it would bring a small systematic offset in the estimate of $A_{\mathrm{H}\alpha}$ by $\sim$10%.

We derive the Hα-based *SFR*s ($SFR_{\mathrm{H}\alpha}$) using the Kennicutt (1998) calibration assuming the Kroupa (2001) IMF:[3]

$$SFR_{\mathrm{H}\alpha} = 5.5 \times 10^{-42}\,L_{\mathrm{H}\alpha}\ [\mathrm{erg\ s^{-1}}]. \qquad (3)$$

We correct here for the dust attenuation effect based on the $A_{\mathrm{H}\alpha}$ estimated above. We also apply aperture correction to the Hα flux based on the difference between the total (petrosian) magnitudes and SDSS fiber magnitudes at the r band (i.e., $m_{r,\,\mathrm{petro}} - m_{r,\,\mathrm{fiber}}$), assuming that the dust attenuation levels measured in the 3″ aperture regions can be applicable to the outer regions. Although this approach might bring some uncertainties, we believe that our simple reproducible approach works reasonably well. We will show a comparison between the $SFR_{\mathrm{H}\alpha}$ derived with this approach

---

[3] We follow Kennicutt et al. (2009) to reduce the *SFR* by a factor of 1.44 to convert the *SFR*s derived under the assumption of the Salpeter (1955) IMF (i.e., the original Kennicutt 1998 prescription) to that derived with the Kroupa (2001) IMF. We apply the same (a factor of 1.44) scaling when we derive SFR_{UV} and SFR_{FIR} in this work.

and the independently measured UV+FIR-based *SFR*s in subsection 2.3 (see also Koyama et al. 2015; Shimakawa et al. 2017; Matsuki et al. 2017), and we will also discuss the potential effects of aperture correction in subsection 3.4.

2.3 UV- and FIR-based *SFR*s and dust attenuation to stellar light

We derive the dust-unobscured part of the *SFR*s from GALEX FUV ($\lambda_{\mathrm{eff}} = 1516$ Å) photometry using Kennicutt (1998) calibration assuming the Kroupa (2001) IMF:

$$SFR_{\mathrm{UV}} = 9.7 \times 10^{-29} L_{\nu,\mathrm{FUV}} \ [\mathrm{erg\,s^{-1}\,Hz^{-1}}]. \tag{4}$$

We use "FUV_MAG_BEST" in the Bianchi et al. (2011) catalog as the total FUV magnitudes, and apply the foreground Galactic extinction correction using the Schlegel, Finkbeiner, and Davis (1998) dust map and the Galactic extinction curve of Cardelli, Clayton, and Mathis (1989) with $R_V = 3.1$. We also apply the *k*-correction by using a *k*-correction tool developed by Chilingarian, Melchior, and Zolotukhin (2010) and Chilingarian and Zolotukhin (2012), where the required correction values are predicted for individual galaxies based on their FUV − NUV and NUV − *g* colors. We note that the *k*-correction values applied to the FUV magnitude of our sample are very small (typically ∼0.02 mag).

We also derive the dust-obscured part of the *SFR*s from AKARI FIR data. Following Koyama et al. (2015), we derive the total infrared luminosity (L_{FIR}) using the *WIDE-S* (90 μm) and *WIDE-L* (140 μm) photometry with the equation established by Takeuchi et al. (2010):

$$\log L_{\mathrm{FIR}} = 0.964 \log L_{\mathrm{AKARI}}^{\mathrm{2band}} + 0.814, \tag{5}$$

where $L_{\mathrm{AKARI}}^{\mathrm{2band}} = \Delta\nu_{90\,\mu\mathrm{m}} L_\nu(90\,\mu\mathrm{m}) + \Delta\nu_{140\,\mu\mathrm{m}} L_\nu(140\,\mu\mathrm{m})$. We note that $\Delta\nu_{90\,\mu\mathrm{m}}$ (=1.47 × 10^{12} [Hz]) and $\Delta\nu_{140\,\mu\mathrm{m}}$ (=0.831 × 10^{12} [Hz]) denote the band widths of the AKARI *WIDE-S* and *WIDE-L* bands, respectively. We realize that 187 out of 2416 galaxies (7.7%) are detected only at *WIDE-S* (90 μm) band, and we remove these sources from our sample (because we cannot estimate their L_{FIR} with the above technique). We do not consider *k*-correction for the FIR photometry as the AKARI band widths are wide enough and its effect is negligible for our $z < 0.1$ galaxy sample. We then use the Kennicutt (1998) equation with the Kroupa (2001) IMF to derive IR-based *SFR*:

$$SFR_{\mathrm{FIR}} = 3.1 \times 10^{-44}(1 - \eta)L_{\mathrm{IR}} \ [\mathrm{erg\,s^{-1}}], \tag{6}$$

where η indicates the fraction of IR emission heated by old stars. We adopt here a constant $\eta = 0.17$ for all our AKARI-detected sources, following the average η value for
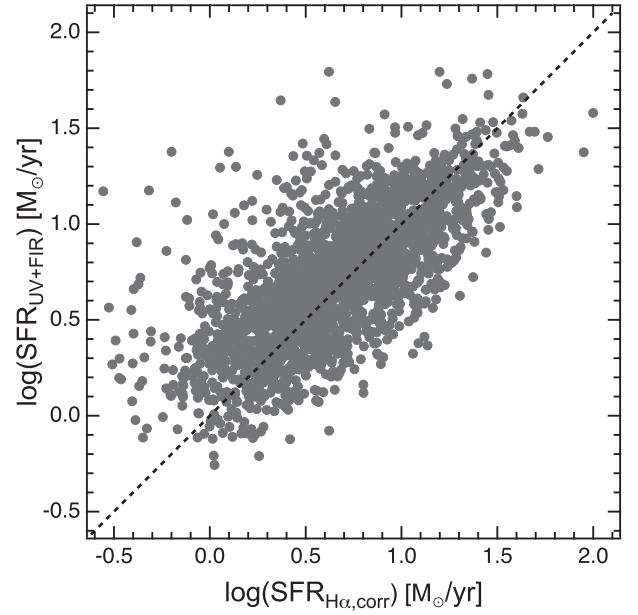

Fig. 2. *SFR*s derived from UV and FIR photometry ($SFR_{\mathrm{UV+FIR}}$) of our new AKARI–SDSS–GALEX sample plotted against their Hα-based *SFR*s with corrections for fiber/aperture effects as well as the dust attenuation effect ($SFR_{\mathrm{H\alpha,\,corr}}$; see text for details). As shown by Koyama et al. (2015) with the older version of the catalog, this plot demonstrates good agreement between the two independently measured *SFR*s.

local star-forming galaxies reported by Buat et al. (2011). We note that the η value could be dependent on the L_{IR} or specific *SFR* of individual galaxies, while the reported η values are different from study to study within a range of η = 0.1–0.4 (e.g., Hirashita et al. 2003; Bell 2003; Buat et al. 2011). We stress that our conclusions are not affected even if we choose different η values. Figure 2 compares $SFR_{\mathrm{UV+FIR}}$ and the dust-corrected $SFR_{\mathrm{H\alpha}}$. Although there exists a relatively large scatter ($\sigma = 0.31$ dex), these two independently measured *SFR*s show good agreement with each other (with a median difference of ∼0.05 dex). We note that we further removed 101 sources (4.5%) having negative aperture correction in the SDSS *r*-band data (with $m_{r,\,\mathrm{fiber}} < m_{r,\,\mathrm{petro}}$), as these galaxies show unrealistically small $SFR_{\mathrm{H\alpha}}$.

Finally, we derive the dust attenuation at FUV (A_{FUV}) as well as the color excess toward stellar light [$E(B - V)_{\mathrm{star}}$] by comparing the total (UV + FIR) *SFR*s and the observed UV-derived *SFR*s (without dust attenuation correction):

$$A_{\mathrm{FUV}} = 2.5 \times \log(SFR_{\mathrm{UV+FIR}}/SFR_{\mathrm{UV}}), \tag{7}$$

$$E(B - V)_{\mathrm{star}} = A_{\mathrm{FUV}}/k_{\mathrm{FUV}}, \tag{8}$$

where we determine k_{FUV} using the Calzetti et al. (2000) reddening curve. In summary, our final AKARI–SDSS–GALEX star-forming galaxy sample includes 2128 sources with the measured *SFR*s and dust attenuation. The source catalog,
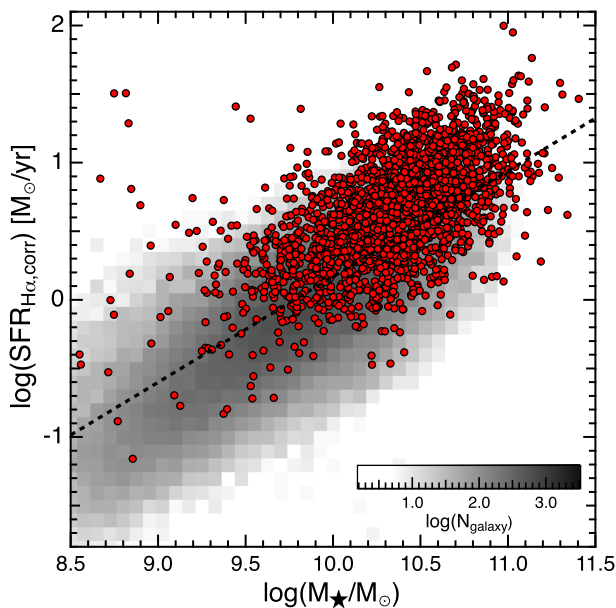
Fig. 3. AKARI(FSCv1)–SDSS–GALEX galaxy sample plotted on an SFR–$M_\star$ diagram (red circles). The gray-scale density plot indicates the distribution of the whole SDSS–GALEX matched SF galaxy sample. To create this plot we divide the panel into 40×40 sub-grids, and compute the number counts of galaxies in each pixel. We note that $M_\star$ and $SFR_{\mathrm{H\alpha, corr}}$ are derived in the same way for both AKARI-detected and undetected sources. (Color online)

as well as our measurements of SFR and dust attenuation for individual sources, will be published on the AKARI website.

2.4 General properties of AKARI-detected galaxies

Because we aim to study the dust attenuation properties of star-forming galaxies with our new AKARI–SDSS–GALEX sample, it is important to understand the fundamental properties and any potential bias associated with the sample. We briefly examine here the nature of the AKARI–SDSS–GALEX sample selected in the previous sections.

In figure 3 we show our new AKARI–SDSS–GALEX galaxies on an SFR–$M_\star$ diagram (red symbols) on top of the distribution of the parent SDSS–GALEX star-forming galaxy sample (gray-scale image plot). Here we use $SFR_{\mathrm{H\alpha, corr}}$ for both AKARI–SDSS–GALEX and SDSS–GALEX samples (as we cannot estimate SFR_{FIR} for galaxies without AKARI detection). As expected, the AKARI-detected sources are relatively massive [mostly with $\log(M_\star/M_\odot) \gtrsim 10.0$], and a highly star-forming population (with $SFR \gtrsim 1\,M_\odot\,\mathrm{yr}^{-1}$). We note that ~7% of the AKARI–SDSS–GALEX galaxies have $>4\times$ higher SFRs with respect to the main sequence (hence starbursts), and so the majority of our samples are massive (normal) star-forming galaxies.

We then plot in figure 4 the Hα dust attenuation ($A_{\mathrm{H\alpha}}$) against their stellar mass (left), SFR (middle), and specific SFR (right). Again, our AKARI–SDSS–GALEX galaxies are shown with the red symbols, while the overall distribution of the SDSS–GALEX sample is shown with the gray-scale image plot. It seems that the distribution of the AKARI–SDSS–GALEX galaxies is similar to that of the whole SDSS–GALEX sample on the $A_{\mathrm{H\alpha}}$–$M_\star$ and $A_{\mathrm{H\alpha}}$–SFR diagrams (except that they are skewed to the massive/high SFR side), while they tend to show high $A_{\mathrm{H\alpha}}$ for their specific SFRs. This is not surprising considering the fact that low-mass galaxies [with $\log(M_\star/M_\odot) \lesssim 10.0$] are not detected at FIR regardless of their specific SFR (figure 3), and those with high specific SFR (but with low $A_{\mathrm{H\alpha}}$) are dominated by low-mass galaxies. We should keep this potential bias in mind, but we believe that our conclusions will not be affected as we will show consistent results in section 5 by using WISE MIR data, which is much deeper in terms of IR-based SFRs.

3 Different dust attenuation toward stellar and nebular regions with the AKARI sample

In figure 5 we compare $E(B - V)_{\mathrm{gas}}$ and $E(B - V)_{\mathrm{star}}$ for our AKARI–SDSS–GALEX sample. It can be seen that there is a positive correlation between $E(B - V)_{\mathrm{gas}}$ and $E(B - V)_{\mathrm{star}}$ with a large scatter. In the left and right panels of figure 5 the color coding indicates stellar mass and specific SFR ($sSFR$) of individual galaxies, respectively; i.e., redder symbols show more massive galaxies in the left panel, while redder symbols indicate lower $sSFR$ in the right panel. We find that galaxies with higher $M_\star$ and/or galaxies with lower specific SFR dominate the upper side of the overall distribution of the data points, suggesting that galaxies with higher $M_\star$ and/or lower $sSFR$ tend to have higher levels of "extra" attenuation toward nebular regions at fixed $E(B - V)_{\mathrm{star}}$. We showed a similar plot in Koyama et al. (2015)—see their figure 14—but we have now confirmed the results using a larger sample size with our updated (deeper) AKARI–SDSS–GALEX catalog.

We now quantify the levels of extra reddening toward nebular regions by calculating the $E(B - V)_{\mathrm{gas}}/E(B - V)_{\mathrm{star}}$ ratio, and study the correlation between $E(B - V)_{\mathrm{gas}}/E(B - V)_{\mathrm{star}}$ and various galaxy properties. In figure 6 we plot the $E(B - V)_{\mathrm{gas}}/E(B - V)_{\mathrm{star}}$ ratio as a function of stellar mass (left), SFR (middle), and $sSFR$ (right). The red circles show the running median in each panel with error bars representing the 25%–75% distribution in each bin. Although the scatter is large in all the panels, the left panel of figure 6 demonstrates the trend that $E(B - V)_{\mathrm{gas}}/$
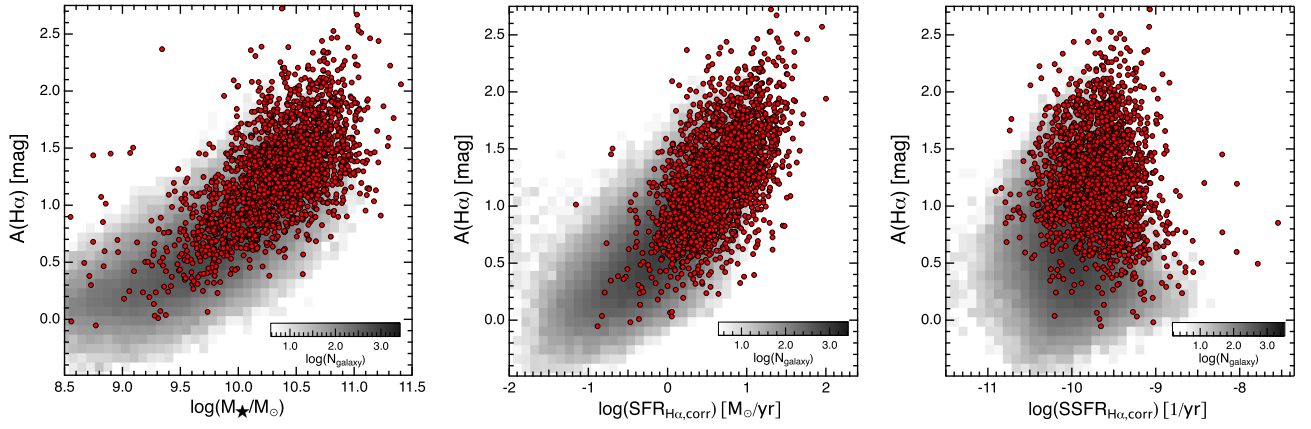
Fig. 4. Dust attenuation at Hα ($A_{H\alpha}$) measured with the Hα/Hβ flux ratio (Balmer decrement) plotted against stellar mass (left), *SFR* (middle), and specific *SFR* (right). The red circles indicate our new AKARI–SDSS–GALEX sample, while the gray-scale density plots show the overall distribution of the SDSS–GALEX matched SF galaxy sample. It can be seen that our AKARI-detected galaxies tend to be a massive, highly star-forming population, and that they are heavily obscured by dust for their specific *SFR*. (Color online)
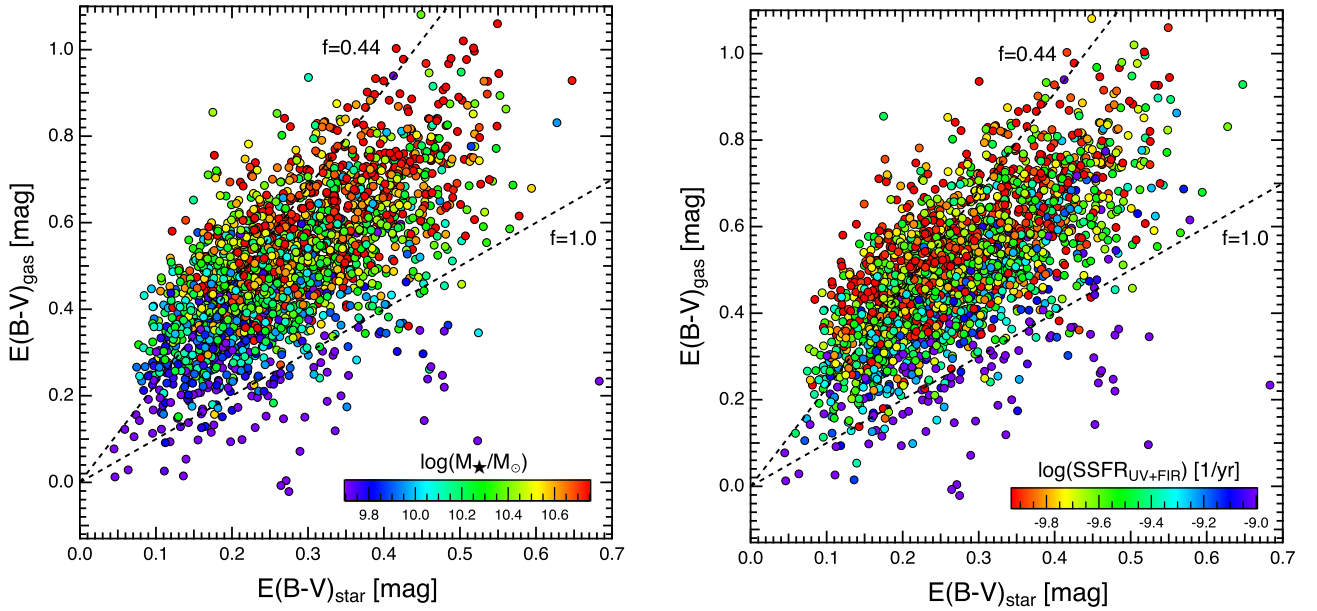
Fig. 5. Comparison between dust reddening to nebular emission [$E(B − V)_{gas}$] and stellar light [$E(B − V)_{star}$] for our AKARI–SDSS–GALEX sample. The color coding indicates stellar mass and specific *SFR* of individual galaxies in the left and right panels, respectively; i.e., redder symbols show more massive galaxies in the left panel, whilst redder symbols indicate lower specific *SFR* in the right panel. We find a trend that galaxies with higher stellar mass and/or lower specific *SFR* tend to be located at the upper side envelope of this correlation—i.e., galaxies with higher stellar mass and/or lower specific *SFR* tend to have higher "extra" attenuation toward nebular regions. The dashed lines drawn in each plot show the relation of $f = E(B − V)_{star}/E(B − V)_{star} = 0.44$ and 1.0 for reference. (Color online)

$E(B − V)_{star}$ increases with increasing stellar mass, consistent with the visual impression that we recognized in figure 5. We therefore conclude that more massive galaxies tend to have higher levels of extra attenuation toward nebular regions, and the best-fit relation between $E(B − V)_{gas}/E(B − V)_{star}$ and the stellar mass of galaxies is provided with the following equation:

$$E(B − V)_{gas}/E(B − V)_{star} = a_0 + a_1 X + a_2 X^2, \qquad (9)$$

where $X = \log(M_\star/10^{10} M_\odot)$, with the best-fit parameters of $a_0 = 1.729 \pm 0.019$, $a_1 = 0.464 \pm 0.039$, and $a_2 = -0.249 \pm 0.048$.

The middle and right panels of figure 6 suggest that $E(B − V)_{gas}/E(B − V)_{star}$ mildly decreases with increasing *SFR*, and as a combination of the trends with stellar mass and *SFR*, we find that $E(B − V)_{gas}/E(B − V)_{star}$ sharply decreases with increasing specific *SFR*, again consistent with the results from figure 5. Our data suggests that
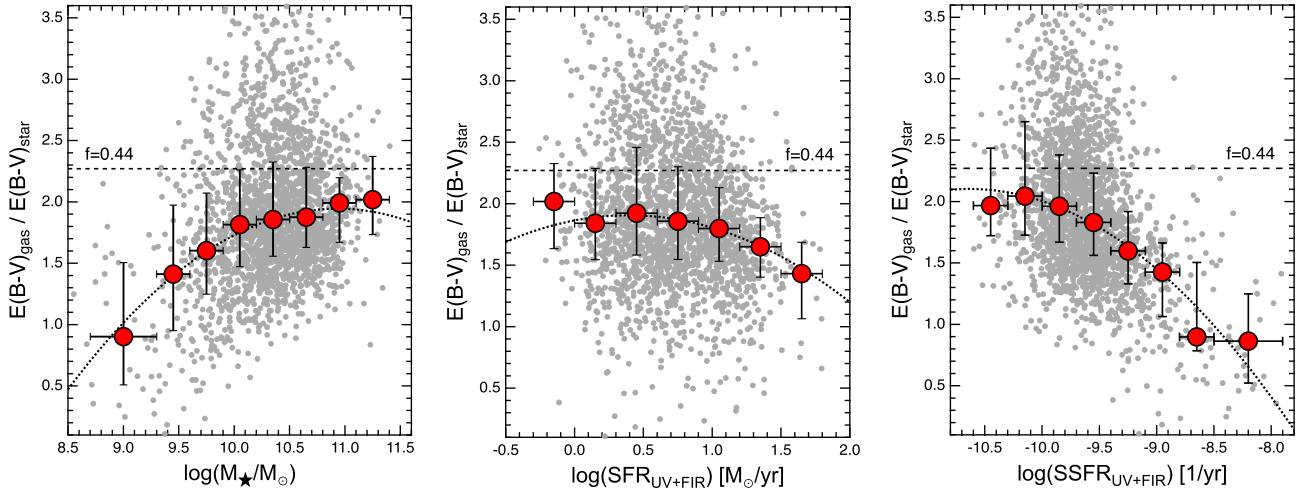
Fig. 6. Extra attenuation toward nebular emission quantified by the $E(B-V)_{gas}/E(B-V)_{star}$ ratio, plotted against stellar mass (left), *SFR* (middle), and specific *SFR* (right) for our AKARI–SDSS–GALEX sample. The gray circles indicate individual AKARI–SDSS–GALEX galaxies, and the red circles with error bars show their median data points computed for a constant 0.3 dex bin, with the *y*-axis error bars representing their 25%–75% distribution. We note that a wider bin size is adopted at the lowest-mass and highest-*sSFR* bins so that each bin has a sufficient (>15) number of galaxies. The error bars on the *x*-axis indicate the adopted bin size. The dotted-line curve drawn in each panel shows the best-fit polynomial function computed for the median data points weighted by $\sigma/\sqrt{N}$ for each bin, and the horizontal dashed line indicates the canonical value of $E(B-V)_{star}/E(B-V)_{gas} = 0.44$ for reference. (Color online)

more actively star-forming galaxies tend to have a lower $E(B-V)_{gas}/E(B-V)_{star}$ ratio, and $E(B-V)_{gas}/E(B-V)_{star}$ becomes consistent with unity at the highest *sSFR* end; i.e., no extra attenuation is required for a very actively star-forming population. By fitting the data points of the running median in the middle and right panels of figure 6, the best-fit relation between $E(B-V)_{gas}/E(B-V)_{star}$ and *SFR* $\{Y = \log(SFR)\ [M_\odot\ \mathrm{yr}^{-1}]\}$ and specific *SFR* $\{Z = \log(sSFR)\ [\mathrm{Gyr}^{-1}]\}$ are provided as follows:

$$E(B-V)_{gas}/E(B-V)_{star} = b_0 + b_1 Y + b_2 Y^2, \qquad (10)$$

$$E(B-V)_{gas}/E(B-V)_{star} = c_0 + c_1 Z + c_2 Z^2, \qquad (11)$$

with the best-fit parameters of $b_0 = 1.865 \pm 0.049$, $b_1 = 0.213 \pm 0.129$, $b_2 = -0.273 \pm 0.079$, $c_0 = 1.450 \pm 0.022$, $c_1 = -0.798 \pm 0.050$, and $c_2 = -0.244 \pm 0.048$. We believe that the above equations can be a convenient tool to provide a realistic estimate of the extra attenuation toward nebular regions [$E(B-V)_{gas}/E(B-V)_{star}$], but we caution that the equations should be used with care, in particular when one needs to use the equation outside the $M_\star/SFR/sSFR$ range shown in figure 6. For example, the equations provide unrealistic "negative" extra attenuation toward nebular regions [i.e., $E(B-V)_{gas}/E(B-V)_{star} < 1$] at the very low-mass end as well as at high specific *SFR* ends. It would be more realistic to assume $E(B-V)_{gas}/E(B-V)_{star} \sim 1$ (hence no extra attenuation to nebular regions) at the low-mass or high-*sSFR* end.

As discussed in section 1, some recent high-redshift studies suggest that the extra attenuation toward nebular regions for high-*z* galaxies is different from that of local galaxies (e.g., Erb et al. 2006; Förster Schreiber et al. 2009; Reddy et al. 2010; Kashino et al. 2013; Tadaki et al. 2013; Wuyts et al. 2013; Pannella et al. 2015; DeBarros et al. 2016—see Puglisi et al. 2016 for a review), but the derived $E(B-V)_{gas}/E(B-V)_{star}$ values are different from study to study, most likely depending on how the parent samples are selected. Our results suggest that the extra attenuation toward nebular regions with respect to that to stellar light significantly changes with stellar mass and/or *sSFR* even for the local galaxies, and it is not surprising to see that the extra attenuation levels are different for high-*z* galaxies because the typical SF activity of high-*z* star-forming galaxies is an order of magnitude higher than those in the present-day universe (e.g., Daddi et al. 2007; Elbaz et al. 2007; Whitaker et al. 2012; Madau & Dickinson 2014).

4 A sanity check with WISE MIR photometry

The main goal of this paper is to use the newly released AKARI Faint Source Catalog ver. 1 and show its scientific capability. It is therefore important to test the validity of the scientific results presented in this work with some independent data set. The Wide-field Infrared Survey Explorer (WISE: Wright et al. 2010) all-sky MIR survey data can be an ideal tool for this purpose, because it can provide independent measurements of IR-based *SFR*s. We use here the

GALEX–SDSS–WISE Legacy Catalog (GSWLC) published by Salim et al. (2016),[4] in which they provide WISE 22 μm-based *SFR*s (SFR_{MIR}) for all galaxies detected at 22 μm by interpolating the Chary and Elbaz (2001) SEDs to match the observed 22 μm flux densities. In this work we use the SFR_{MIR} from the 22 μm flux in the "unWISE" catalog (Lang et al. 2016) recommended for low-z galaxies with large apparent size (see Salim et al. 2016). We note that Salim et al. (2016) assumed a Chabrier (2003) IMF when deriving the SFR_{MIR}, and we therefore rescale their SFR_{MIR} (by +0.03 dex) to account for the IMF difference.

Following the same strategy as performed in subsection 2.1 to construct our AKARI–SDSS–GALEX catalog, we first match our SDSS–GALEX star-forming galaxy sample (at $0.02 < z < 0.1$) with the "GSWLC-X" catalog.[5] We reconstruct the WISE–SDSS–GALEX catalog by matching our own SDSS–GALEX sample with the GSWLC catalog, to keep consistency in the data release versions of the SDSS and GALEX catalog used for the analyses. We restrict the sample to those detected at the WISE 22 μm band, and now we identify 50353 WISE–SDSS–GALEX samples for which MIR-based *SFR*s are available. By matching the WISE–SDSS–GALEX sample with our AKARI–SDSS–GALEX sample constructed in subsection 2.1, we find that 2036 sources (>95%) of the AKARI–SDSS–GALEX sample are also identified in the WISE–SDSS–GALEX sample constructed here.

In figure 7 we compare the FIR-based *SFR*s (derived with AKARI data in subsection 2.2) and WISE 22 μm-based *SFR*s (provided by Salim et al. 2016, after accounting for the IMF difference) for galaxies identified in both the AKARI and WISE catalogs, showing a reasonable agreement between UV+FIR and UV+MIR *SFR*s (with a median difference of 0.01 dex and a scatter of $\sigma = 0.22$ dex). Following the good agreement between the FIR- and MIR-based *SFR*s, we will perform the same analysis presented in the previous sections with a significantly larger number of galaxies in the WISE–SDSS–GALEX sample.

We apply the same method as in subsection 2.2 to derive $E(B-V)_{star}$ from SFR_{FIR} and SFR_{UV}, and we now calculate $A_{UV, WISE}$ and $E(B-V)_{star, WISE}$ with the following equations:

$$A_{FUV, WISE} = 2.5 \times \log(SFR_{UV+MIR}/SFR_{UV}), \quad (12)$$

[4] ⟨https://archive.stsci.edu/prepds/gswlc/⟩.

[5] We note that Salim et al. (2016) published three versions of the catalog (GSWLC-A, M, D) depending on the GALEX survey depths used for the source matching, and they also published a master catalog (GSWLC-X) in which they exploited the deepest data among GSWLC-A, M, and D. We decided to use "GSWLC-X," which covers the largest fraction of the SDSS survey area (see Salim et al. 2016 for more details).
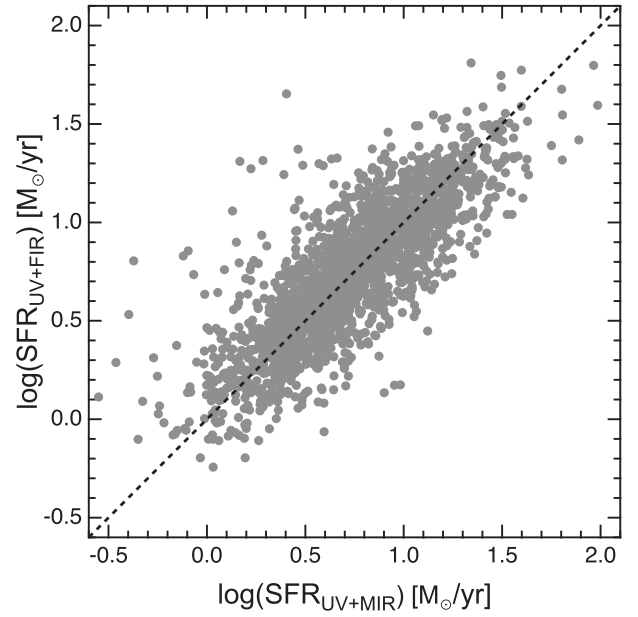
Fig. 7. *SFR*s derived from AKARI FIR photometry (subsection 2.2) plotted against *SFR*s from WISE 22 μm data taken from the public GSWLC catalog by Salim et al. (2016) for galaxies identified in both our AKARI–SDSS–GALEX sample and the GSWLC catalog, taking into account the different IMF assumptions. The two *SFR* measurements show good agreement with each other.

$$E(B-V)_{star, WISE} = A_{FUV, WISE}/k_{FUV}. \quad (13)$$

In figure 8 we compare $E(B-V)_{gas}$ and $E(B-V)_{star, WISE}$, with color coding based on the stellar mass and specific *SFR* of the galaxies. This is the same plot as figure 5, but considering the large sample size of the WISE–SDSS–GALEX sources, we show here the average $M_\star$ (left panel) and specific *SFR* (right panel) at each position on this diagram, rather than showing the individual data points. This plot clearly demonstrates that galaxies with higher stellar mass or lower specific *SFR* tend to have higher $E(B-V)_{gas}$ at fixed $E(B-V)_{star}$, confirming the trend we reported in figure 5 using the AKARI–SDSS–GALEX sample.

We then quantify the extra reddening toward nebular regions by computing the $E(B-V)_{gas}/E(B-V)_{star, WISE}$ ratio (as we did in the previous section), and we plot in figure 9 the derived $E(B-V)_{gas}/E(B-V)_{star, WISE}$ against stellar mass (left), *SFR* (middle), and *sSFR* (right) for all the WISE–SDSS–GALEX galaxies. Instead of showing the individual data points, we show the distribution of all WISE–SDSS–GALEX galaxies with the gray-scale density plot, and we show the running median with the orange squares with error bars (indicating the 25%–75% distribution in each bin). It can be seen that the extra attenuation level increases with increasing stellar mass, while it
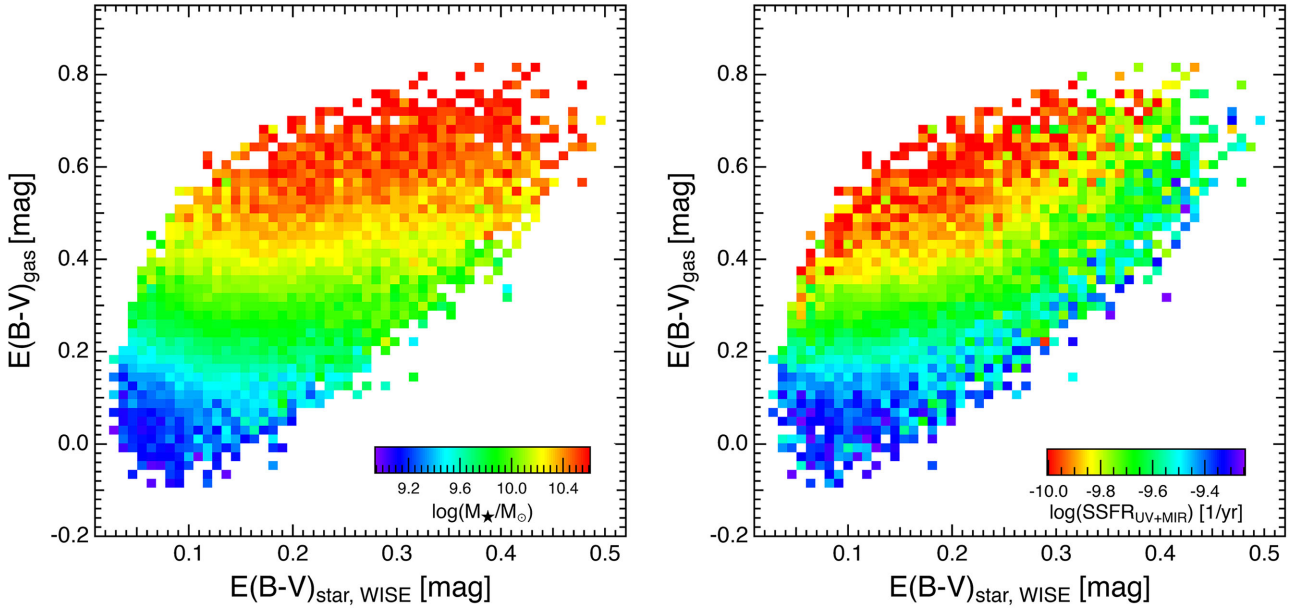
Fig. 8. $E(B-V)_{gas}$ versus $E(B-V)_{star}$ plot for the SDSS–GALEX–WISE matched sample, with color coding based on stellar mass (left) and specific *SFR* (right). To create this plot we divide the panels into 60×60 sub-grids and compute the average stellar mass and *sSFR* at each pixel. We require a minimum sample size of $N_{galaxy} = 4$ to compute the average stellar mass in this diagram. We follow this strategy when we create the similar color-image plots in the following sections. This plot confirms the trend reported in figure 5 with the larger sample; i.e., galaxies with higher $M_\star$ and/or with lower specific *SFR* tend to have higher $E(B-V)_{gas}$ at fixed $E(B-V)_{star}$. (Color online)
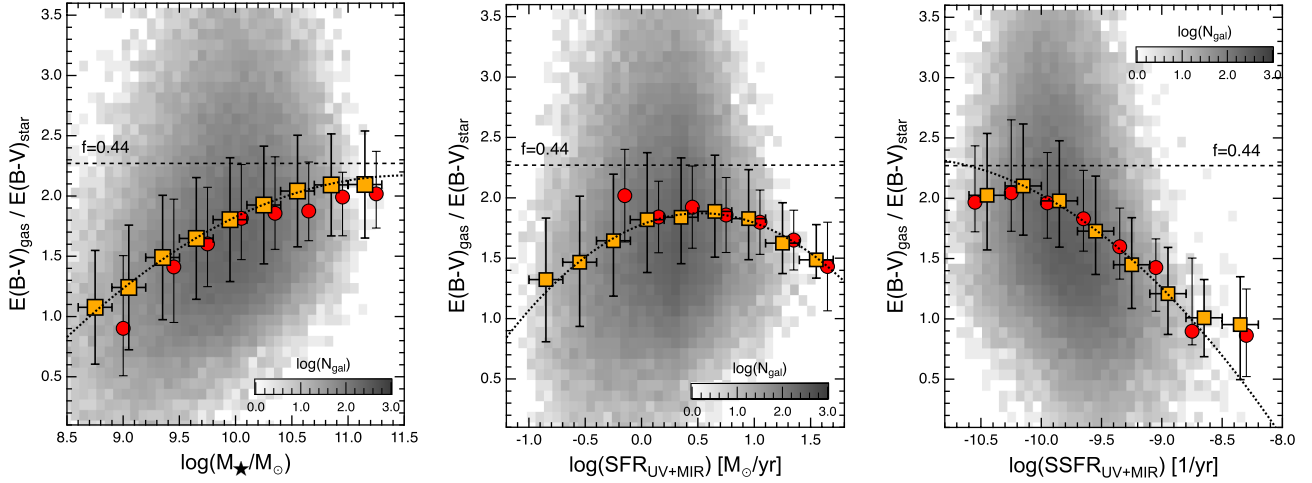
Fig. 9. Same plot as figure 6 to show the extra attenuation levels as a function of various properties for the SDSS–GALEX–WISE sample. Because of the very large number of data points, we show their distribution by gray-scale density plot, instead of showing the individual data points on these plots. The orange squares with error bars show the running median (with 25%–75% distribution), and the best-fit third-order polynomial function curve is also shown in each panel. The horizontal error bars represent the 0.3 dex bin size applied for all the calculations in this diagram, where all the sub-samples have a sufficient number of galaxies (>50). The median data points plotted in figure 6 (derived with AKARI data) are also shown with the red circles, showing good agreement with the results using WISE data, and the canonical $E(B-V)_{star}/E(B-V)_{gas} = 0.44$ line is drawn for reference. (Color online)

decreases with increasing *sSFR*, consistent with the results we reported in figure 6.

The trend for *SFR* seems to be different from that shown in figure 6; we showed a mild *decrease* of the $E(B-V)_{gas}/E(B-V)_{star}$ ratio with increasing *SFR* in figure 6, while in figure 9 $E(B-V)_{gas}/E(B-V)_{star}$ increases at $\log(SFR) \lesssim -1.0$–0.5 [$M_\odot$ yr^{-1}] and decreases at $\log(SFR)$ $\gtrsim$ 0.5–1.5 [$M_\odot$ yr^{-1}]. However, it should be noted that the *SFR* ranges presented in figure 6 and figure 9 are different. As we showed in subsection 3.1, most of the AKARI-detected samples have $\log(SFR) \gtrsim 0$ [$M_\odot$ yr^{-1}], whilst the WISE data goes an order of magnitude deeper than the AKARI data in terms of IR-based *SFR*. We note that the mild decrease of the $E(B-V)_{gas}/E(B-V)_{star, \text{WISE}}$
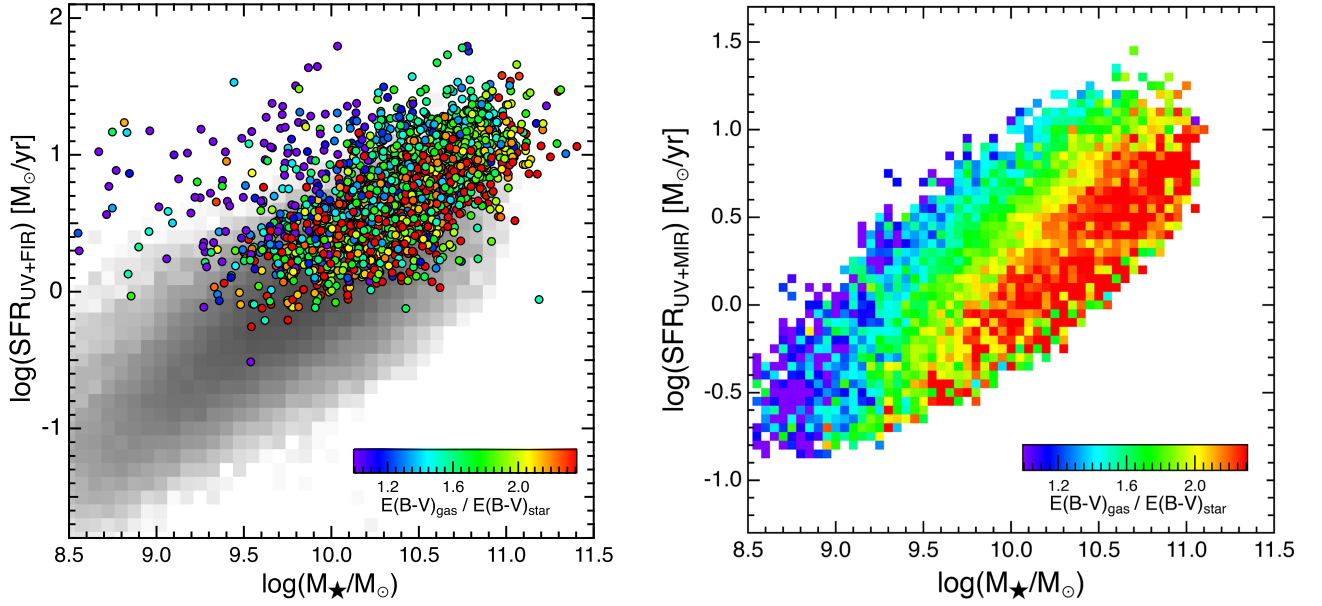
Fig. 10. Extra attenuation toward nebular regions across the SFR–$M_\star$ diagram for the AKARI–SDSS–GALEX sample (left) and for the WISE–SDSS–GALEX sample (right). In the left panel we show the individual data points of the AKARI–SDSS–GALEX sample with color coding indicating the $E(B - V)_{\rm gas}/E(B - V)_{\rm star}$ ratio, and the gray-scale density plot shows the distribution of the parent SDSS–GALEX sample (same as figure 3). For the right panel we compute the average $E(B - V)_{\rm gas}/E(B - V)_{\rm star}$ ratio of the WISE–SDSS–GALEX sample at each position on this diagram by dividing each panel into 60×60 sub-grids. We note that we require here a minimum sample size of $N_{\rm galaxy} = 4$ for each pixel, and thus the data points seen at the top-left corner of the left panel (i.e., low-mass galaxies with high SFR) are not seen in the right panel. The two plots are broadly consistent with each other in the sense that the $E(B - V)_{\rm gas}/E(B - V)_{\rm star}$ ratio becomes largest at the low-SFR side. (Color online)

ratio toward the high SFR end seen in figure 6 is consistent with our current analysis using WISE data (see the red circles in figure 9 showing the same data points as in figure 6). The reason for this different behavior at the low-SFR and high-SFR sides is unclear, but we speculate that the $E(B - V)_{\rm gas}/E(B - V)_{\rm star}$ ratio increases following the increase of stellar mass at the low-SFR side, while the effect of specific SFR becomes stronger at the high-SFR end (the trend with stellar mass becomes almost flat at the high-$M_\star$ end, as shown in the left panel of figure 9).

5 Extra attenuation toward nebular regions across star-forming main sequence

We have shown that the extra dust attenuation toward nebular regions changes with stellar mass and (specific) SFR. In this section we study how the $E(B - V)_{\rm gas}/E(B - V)_{\rm star}$ ratio changes across the SFR–$M_\star$ diagram. In figure 10 we show the SFR–$M_\star$ diagram for the AKARI–SDSS–GALEX sample (left) and for the WISE–SDSS–GALEX sample (right) with color coding based on the $E(B - V)_{\rm gas}/E(B - V)_{\rm star}$ ratio. For the right panel of this plot we divide the diagram into 60×60 sub-grids and compute the average $E(B - V)_{\rm gas}/E(B - V)_{\rm star}$ at each pixel (with the requirement of a minimum sample size of $N_{\rm galaxy} = 4$ in each pixel). Both of these plots demonstrate that, at fixed stellar mass, there remains

a trend that galaxies with *lower sSFR* tend to have a *higher* $E(B - V)_{\rm gas}/E(B - V)_{\rm star}$ ratio; i.e., galaxies located at the lower side of the star-forming main sequence tend to suffer from higher extra attenuation toward nebular regions.

Assuming that the levels of extra attenuation toward nebular regions with respect to the stellar continuum light reflects the different geometry of stars and gas/dust within the galaxies, as argued by many authors (e.g., Calzetti 1997; Price et al. 2014; Reddy et al. 2015), the fact that the $E(B - V)_{\rm gas}/E(B - V)_{\rm star}$ ratio changes across the SFR–$M_\star$ diagram suggests that the geometry of stars and dust within the galaxies becomes more and more different as the SF quenching process proceeds. In other words, the distribution of star-forming regions becomes more distinct (patchy and/or centrally concentrated) from the distribution of stellar components.

To study the nature of galaxies with high $E(B - V)_{\rm gas}/E(B - V)_{\rm star}$ ratios, we show in figure 11 the attenuation at FUV measured with the $L_{\rm IR}/L_{\rm UV}$ ratio plotted against the FUV − NUV colors (equivalent to the so-called "IRX–β" diagram; e.g., Meurer et al. 1999; Witt & Gordon 2000; Takeuchi et al. 2010; Reddy et al. 2010; Buat et al. 2011), with color coding based on the extra reddening toward nebular regions, $E(B - V)_{\rm gas}/E(B - V)_{\rm star}$. We show individual data points for the AKARI–SDSS–GALEX sample, while we show the average
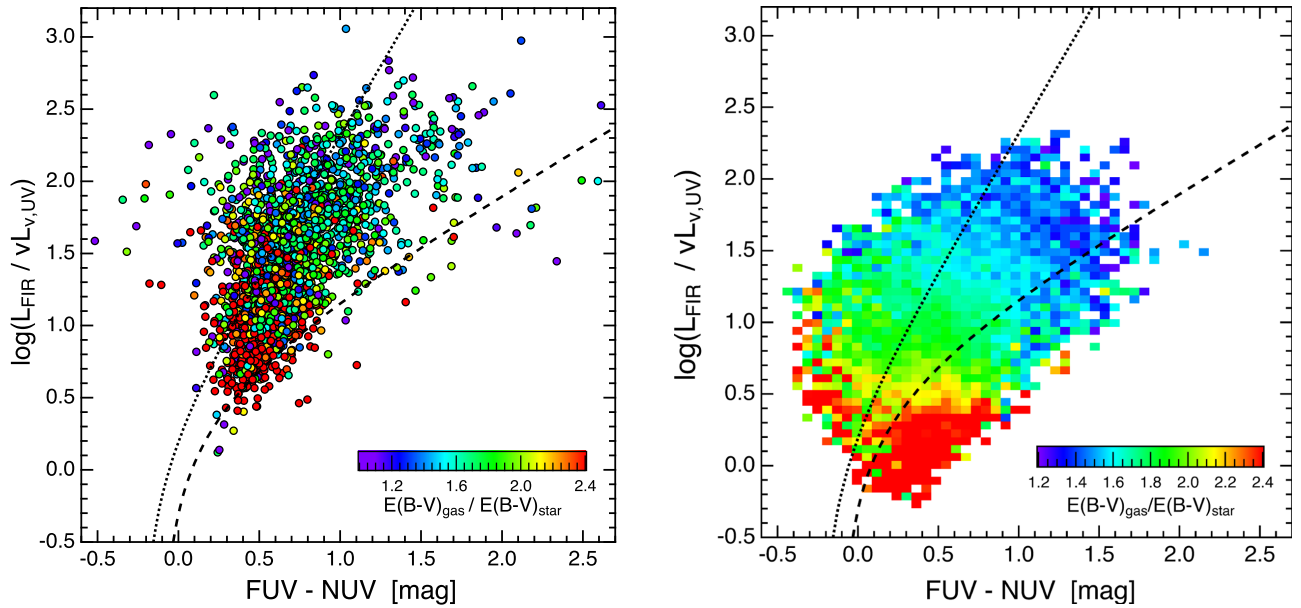
Fig. 11. Attenuation at FUV (quantified by the $SFR_{\rm UV+FIR}/SFR_{\rm UV}$ or $SFR_{\rm UV+MIR}/SFR_{\rm UV}$ ratios) plotted against FUV − NUV colors (corresponding to the UV slope) for the AKARI–SDSS–GALEX sample (left) and the WISE–SDSS–GALEX star-forming galaxy sample (right), with the color code indicating the extra reddening toward nebular regions, $E(B-V)_{\rm gas}/E(B-V)_{\rm star}$, in both cases. The dotted-line and dashed-line curves shown in the plots indicate the relation for starburst galaxies by Meurer, Heckman, and Calzetti (1999)—see also Takeuchi et al. 2010—and that of more normal star-forming galaxies established by Boissier et al. (2007), respectively. Dusty starburst galaxies showing stronger IR excess tend to have *lower* extra attenuation toward nebular regions, consistent with the results reported in figure 10. (Color online)

of the $E(B-V)_{\rm gas}/E(B-V)_{\rm star}$ ratio at each pixel for the WISE–SDSS–GALEX sample. This plot demonstrates that galaxies with "IR excess" sources (i.e., dusty galaxies) tend to have a *lower* $E(B-V)_{\rm gas}/E(B-V)_{\rm star}$ ratio, suggesting that the FIR light and the ionized gas emission lines are coming from the same (star-forming) regions within the galaxies. On the other hand, galaxies with a high $E(B-V)_{\rm gas}/E(B-V)_{\rm star}$ ratio are strongly clustered at the low $L_{\rm IR}/L_{\rm UV}$ side, demonstrating that galaxies with a higher $E(B-V)_{\rm gas}/E(B-V)_{\rm star}$ ratio tend to be less dusty with a moderate star-forming population, consistent with the results shown in figure 10.

6 Caveats on the use of $SFR_{\rm H\alpha}$ instead of $SFR_{\rm UV+IR}$, and other uncertainties

In figure 12 we show the same SFR–$M_\star$ plot as figure 10 by replacing the $SFR_{\rm UV+FIR}$ (or $SFR_{\rm UV+MIR}$) with the Hα-derived SFRs. It can be seen that the region showing the highest levels of extra reddening [with $E(B-V)_{\rm gas}/E(B-V)_{\rm star} \gtrsim 2$; i.e., red-colored regions in the plot] is strongly concentrated at the very massive end [log $(M_\star/M_\odot)$ > 10.5], whilst we reported in figure 10 that the red-colored regions are distributed along the bottom part of the SF main sequence over a wide stellar mass range. The physical reason for the different behavior between $SFR_{\rm UV+MIR}$ and $SFR_{\rm H\alpha,\,corr}$ is unclear, but we speculate that it originates
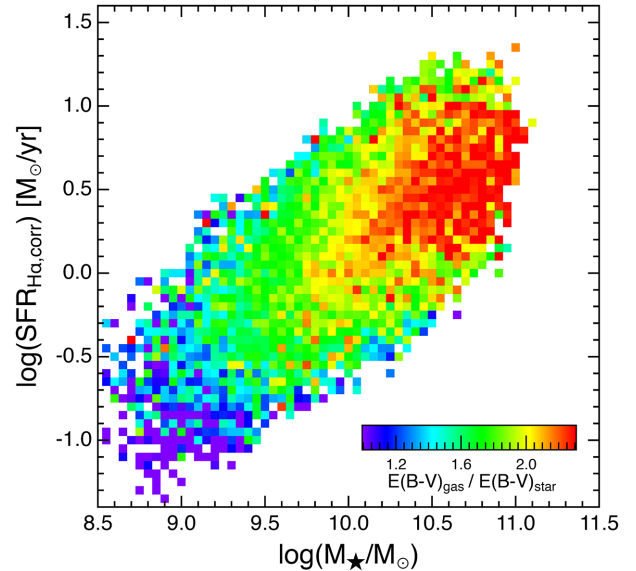

Fig. 12. Same plot as figure 10, but here we use Hα-based SFRs instead of UV+IR SFRs. In this plot it can be seen that the $E(B-V)_{\rm gas}/E(B-V)_{\rm star}$ ratio is higher at the massive end, with log $(M_\star/M_\odot) \gtrsim 10.5$, while the visual impression on the trend across the SF main sequence is slightly different from that of figure 10, particularly at the low-mass/low-SFR end (see text for more details). (Color online)

from disagreement between $SFR_{\rm UV+MIR}$ and $SFR_{\rm H\alpha,\,corr}$ at the low-mass end. We investigate this possibility in figure 13 by comparing $SFR_{\rm H\alpha,\,corr}$ and $SFR_{\rm UV+MIR}$, with the color code indicating the $E(B-V)_{\rm gas}/E(B-V)_{\rm star}$ ratio. It can be seen

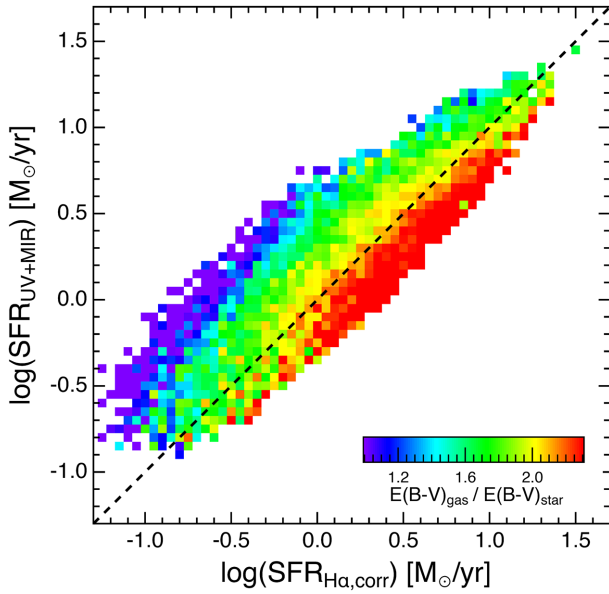**Fig. 13.** Average extra reddening toward nebular regions, $E(B-V)_{gas}/E(B-V)_{star}$, at each position on the $SFR_{H\alpha}$–SFR_{UV+MIR} diagram. There is a clear trend that galaxies showing $SFR_{H\alpha} > SFR_{UV+MIR}$ tend to have higher levels of $E(B-V)_{gas}/E(B-V)_{star}$. (Color online)

that galaxies with $SFR_{H\alpha,\,corr} > SFR_{UV+MIR}$ tend to show significantly higher levels of extra attenuation.

We caution that the major source of uncertainties in our analysis would be the dust attenuation correction (and aperture correction) when we derive Hα-based SFRs. We performed a simple dust attenuation correction assuming that the distribution of Hα and Hβ line fluxes follow that of stellar continuum light measured in the r band (subsection 2.2). In figure 14 we briefly test the effects of aperture correction by creating the same plots as figures 10, 12, and 13 with the color code (gray scale) indicating the average aperture correction at each position on these diagrams ($m_{r,\,fiber} - m_{r,\,petro}$). It can be seen that low-mass galaxies [$\log(M_\star/M_\odot) \lesssim 10$] with low SFR tend to require larger aperture correction, mainly because they are intrinsically faint sources and we can detect those low-mass, low-SFR galaxies only when they are located in the very nearby universe (hence with large apparent size). It should be noted that we need to apply $\sim 2\,mag$ or more aperture correction when we derive $SFR_{H\alpha}$ for these low-mass, low-SFR galaxies. We note that the amount of aperture correction is not directly linked to the uncertainties in the derived SFR, but it might be unrealistic to assume completely uniform dust attenuation levels over the galaxies (e.g., Kreckel et al. 2013; Hemmati et al. 2015; Nelson et al. 2016; Tacchella et al. 2018), and therefore our results at the low-mass/low-SFR end should be interpreted with care.

Finally, we comment that another source of uncertainty is regarding the choice of dust attenuation curves. In particular, we should note that the results must be interpreted with care in case one applies a variable attenuation curve depending on galaxy properties (e.g., Kriek & Conroy 2013; Salim et al. 2018). A recent study by Salim, Boquien, and Lee (2018) suggests that lower-mass galaxies or galaxies with low specific SFR tend to have steeper attenuation curve slopes. For those galaxies with steeper slopes, the observed UV attenuation tends to be translated into smaller $E(B-V)_{star}$ [and hence a higher $E(B-V)_{gas}/E(B-V)_{star}$ ratio]. This is qualitatively consistent with our results, and may partly explain the trend reported in this work that the $E(B-V)_{gas}/E(B-V)_{star}$ ratio is higher for galaxies below the SF main sequence. We believe that our conclusions are robust because most of the results are unchanged even if we use $SFR_{H\alpha}$ or SFR_{UV+IR}, but more detailed, systematic, spatially resolved studies for a statistical sample of galaxies selected from above/below the SF main sequence would be needed to obtain more conclusive evidence for the changing star/dust geometry as well as the changing dust attenuation curve across the SFR–$M_\star$ diagram.

7 Summary

In this study we constructed an updated version of our AKARI–SDSS–GALEX star-forming galaxy catalog at $0.02 < z < 0.10$ using the newly released AKARI/FIS all-sky Faint Source Catalog ver. 1 (FSCv1). With the improved sensitivity of the Faint Source Catalog, the number of matched sources is increased by a factor of $\sim 2\times$ compared to the previous version of the catalog presented by Koyama et al. (2015) using the AKARI Bright Source Catalog (ver. 1).

We derived SFRs from dust-corrected Hα luminosities and from UV+FIR luminosities, and find a reasonable agreement between the two independent measurements of SFRs. We then derived the dust attenuation levels toward stellar light (from the IR/UV ratio, SFR_{UV+FIR}/SFR_{UV}) and nebular emission lines (from the Hα/Hβ ratio), to discuss the different dust attenuation levels toward stellar and nebular regions within local star-forming galaxies. We quantify the "extra" attenuation toward nebular regions by the $E(B-V)_{gas}/E(B-V)_{star}$ ratio, and find that the levels of extra attenuation increases with increasing stellar mass, while it decreases with increasing $sSFR$. At the high specific SFR end, no extra reddening is required [i.e., $E(B-V)_{gas}/E(B-V)_{star} \approx 1$].

If we assume that the different levels of dust attenuation toward stellar and nebular regions is attributed to the different star/dust geometry within the galaxies, as often
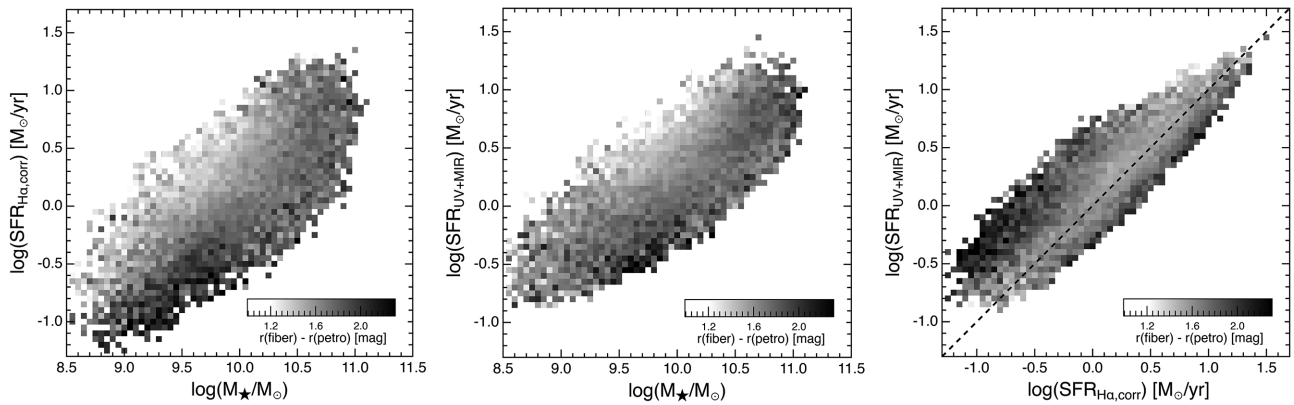
Fig. 14. Same plot as figures 10, 12, and 13, but here the color coding (gray scale) indicates the average aperture correction ($r_{fiber} - r_{petro}$) applied for the galaxies in each pixel, to examine the potential effects of aperture correction. From the left and middle panels it can be seen that low-mass galaxies with low *SFR* tend to require relatively large aperture correction, hence potentially accompanying a large uncertainty. In the right panel it can be recognized that galaxies showing strong IR excess (with $SFR_{UV+MIR} > SFR_{H\alpha, corr}$) also tend to require larger aperture correction.

argued by previous studies, we suggest that more massive galaxies tend to have more patchy (or centrally concentrated) distribution of dust within the galaxies, while the H II regions tend to be more uniformly distributed over the galaxies in low-mass galaxies (or those with high specific *SFR*s). Our results are also confirmed by using the WISE 22 μm photometry with the GSWLC catalog published by Salim et al. (2016).

We then studied how the extra attenuation toward nebular regions, $E(B - V)_{gas}/E(B - V)_{star}$, changes on the *SFR*–$M_\star$ diagram, using the AKARI–SDSS–GALEX and WISE–SDSS–GALEX samples. We find that, even at a fixed stellar mass, there is a clear trend that galaxies located *below* the star-forming main sequence tend to have higher levels of extra attenuation, suggesting that the change in the $E(B - V)_{gas}/E(B - V)_{star}$ ratio is related to the galaxy transition or SF quenching process, and that the distribution of stars and dust becomes more and more different as the SF quenching process proceeds.

Our results based on the new AKARI FSCv1, helped by SDSS, GALEX, and WISE data, demonstrate interesting trends between the $E(B - V)_{gas}/E(B - V)_{star}$ ratio and various galaxy properties. However, considering the potential large uncertainty regarding the derivation of Hα *SFR* (which is inevitable as long as we rely on the SDSS data), more detailed, systematic, spatially resolved studies for a statistical sample of galaxies selected from above/below the SF main sequence would be necessary to obtain conclusive evidence of the change in the dust geometry across the *SFR*–$M_\star$ diagram.

Acknowledgments

References

Abazajian, K. N., et al. 2009, ApJS, 182, 543
Baldwin, J. A., Phillips, M. M., & Terlevich, R. 1981, PASP, 93, 5

Bell, E. F. 2003, ApJ, 586, 794

Bianchi, L., Efremova, B., Herald, J., Girardi, L., Zabot, A., Marigo, P., & Martin, C. 2011, MNRAS, 411, 2770

Boissier, S., et al. 2007, ApJS, 173, 524

Buat, V., Giovannoli, E., Takeuchi, T. T., Heinis, S., Yuan, F.-T., Burgarella, D., Noll, S., & Iglesias-Páramo, J. 2011, A&A, 529, A22

Calzetti, D. 1997, AJ, 113, 162

Calzetti, D., Armus, L., Bohlin, R. C., Kinney, A. L., Koornneef, J., & Storchi-Bergmann, T. 2000, ApJ, 533, 682

Calzetti, D., Kinney, A. L., & Storchi-Bergmann, T. 1994, ApJ, 429, 582

Cardelli, J. A., Clayton, G. C., & Mathis, J. S. 1989, ApJ, 345, 245

Chabrier, G. 2003, PASP, 115, 763

Charlot, S., & Fall, S. M. 2000, ApJ, 539, 718

Chary, R., & Elbaz, D. 2001, ApJ, 556, 562

Chilingarian, I. V., Melchior, A.-L., & Zolotukhin, I. Y. 2010, MNRAS, 405, 1409

Chilingarian, I. V., & Zolotukhin, I. Y. 2012, MNRAS, 419, 1727

Daddi, E., et al. 2007, ApJ, 670, 156

De Barros, S., Reddy, N., & Shivaei, I. 2016, ApJ, 820, 96

Doi, Y., et al. 2015, PASJ, 67, 50

Elbaz, D., et al. 2007, A&A, 468, 33

Erb, D. K., Steidel, C. C., Shapley, A. E., Pettini, M., Reddy, N. A., & Adelberger, K. L. 2006, ApJ, 647, 128

Förster Schreiber, N. M., et al. 2009, ApJ, 706, 1364

Garn, T., et al. 2010, MNRAS, 402, 2017

Garn, T., & Best, P. N. 2010, MNRAS, 409, 421

Geach, J. E., Smail, I., Best, P. N., Kurk, J., Casali, M., Ivison, R. J., & Coppin, K. 2008, MNRAS, 388, 1473

Hao, C.-N., Kennicutt, R. C., Johnson, B. D., Calzetti, D., Dale, D. A., & Moustakas, J. 2011, ApJ, 741, 124

Hemmati, S., Mobasher, B., Darvish, B., Nayyeri, H., Sobral, D., & Miller, S. 2015, ApJ, 814, 46

Hirashita, H., Buat, V., & Inoue, A. K. 2003, A&A, 410, 83

Kashino, D., et al. 2013, ApJ, 777, L8

Kauffmann, G., et al. 2003, MNRAS, 341, 33

Kauffmann, G., et al. 2003, MNRAS, 346, 1055

Kawada, M., et al. 2007, PASJ, 59, S389

Kennicutt, R. C., Jr. 1998, ApJ, 498, 541

Kennicutt, R. C., Jr., et al. 2009, ApJ, 703, 1672

Kennicutt, R. C., Jr., & Evans, N. J., II 2012, ARA&A, 50, 531

Kewley, L. J., Groves, B., Kauffmann, G., & Heckman, T. 2006, MNRAS, 372, 961

Koyama, Y., et al. 2013, MNRAS, 434, 423

Koyama, Y., et al. 2015, MNRAS, 453, 879

Koyama, Y., Kodama, T., Shimasaku, K., Hayashi, M., Okamura, S., Tanaka, I., & Tokoku, C. 2010, MNRAS, 403, 1611

Kreckel, K., et al. 2013, ApJ, 771, 62

Kriek, M., & Conroy, C. 2013, ApJ, 775, L16

Kroupa, P. 2001, MNRAS, 322, 231

Lang, D., Hogg, D. W., & Schlegel, D. J. 2016, AJ, 151, 36

Madau, P., & Dickinson, M. 2014, ARA&A, 52, 415

Martin, D. C., et al. 2005, ApJ, 619, L1

Matsuki, Y., Koyama, Y., Nakagawa, T., & Takita, S. 2017, MNRAS, 466, 2517

Meurer, G. R., Heckman, T. M., & Calzetti, D. 1999, ApJ, 521, 64

Murakami, H., et al. 2007, PASJ, 59, S369

Nelson, E. J., et al. 2016, ApJ, 817, L9

Pannella, M., et al. 2015, ApJ, 807, 141

Poggianti, B. M., & Wu, H. 2000, ApJ, 529, 157

Price, S. H., et al. 2014, ApJ, 788, 86

Puglisi, A., et al. 2016, A&A, 586, A83

Reddy, N. A., et al. 2015, ApJ, 806, 259

Reddy, N. A., Erb, D. K., Pettini, M., Steidel, C. C., & Shapley, A. E. 2010, ApJ, 712, 1070

Salim, S., et al. 2007, ApJS, 173, 267

Salim, S., et al. 2016, ApJS, 227, 2

Salim, S., Boquien, M., & Lee, J. C. 2018, ApJ, 859, 11

Salpeter, E. E. 1955, ApJ, 121, 161

Schlegel, D. J., Finkbeiner, D. P., & Davis, M. 1998, ApJ, 500, 525

Shimakawa, R., Koyama, Y., Prochaska, J. X., Guo, Y., Tadaki, K., & Kodama, T. 2017, arXiv:1705.01127

Shivaei, I., et al. 2015, ApJ, 815, 98

Shivaei, I., Reddy, N. A., Steidel, C. C., & Shapley, A. E. 2015, ApJ, 804, 149

Sobral, D., Best, P. N., Matsuda, Y., Smail, I., Geach, J. E., & Cirasuolo, M. 2012, MNRAS, 420, 1926

Sobral, D., Smail, I., Best, P. N., Geach, J. E., Matsuda, Y., Stott, J. P., Cirasuolo, M., & Kurk, J. 2013, MNRAS, 428, 1128

Steidel, C. C., et al. 2014, ApJ, 795, 165

Tacchella, S., et al. 2018, ApJ, 859, 56

Tadaki, K., Kodama, T., Tanaka, I., Hayashi, M., Koyama, Y., & Shimakawa, R. 2013, ApJ, 778, 114

Takeuchi, T. T., Buat, V., Heinis, S., Giovannoli, E., Yuan, F.-T., Iglesias-Páramo, J., Murata, K. L., & Burgarella, D. 2010, A&A, 514, A4

Takita, S., et al. 2015, PASJ, 67, 51

Theios, R. L., Steidel, C. C., Strom, A. L., Rudie, G. C., Trainor, R. F., & Reddy, N. A. 2018, arXiv:1805.00016

Whitaker, K. E., van Dokkum, P. G., Brammer, G., & Franx, M. 2012, ApJ, 754, L29

Wild, V., Charlot, S., Brinchmann, J., Heckman, T., Vince, O., Pacifici, C., & Chevallard, J. 2011, MNRAS, 417, 1760

Witt, A. N., & Gordon, K. D. 2000, ApJ, 528, 799

Wright, E. L., et al. 2010, AJ, 140, 1868

Wuyts, S., et al. 2013, ApJ, 779, 135

Yamamura, I., Makiuti, S., Ikeda, N., Fukuda, Y., Oyabu, S., Koga, T., & White, G. J. 2010, VizieR Online Data Catalog, II/298

Zahid, H. J., Kudritzki, R.-P., Conroy, C., Andrews, B., & Ho, I.-T. 2017, ApJ, 847, 18